Electrochimica Acta 443 (2023) 141935

Contents lists available at ScienceDirect

Electrochimica Acta

journal homepage: www.journals.elsevier.com/electrochimica-acta

Reduced hysteresis and enhanced air stability of low-temperature processed carbon-based perovskite solar cells by surface modification

Soe Ko Ko Aung [a,b], Anuja Vijayan [b], Masoud Karimipour [b,c,d], Tosawat Seetawan [a], Gerrit Boschloo [b,*]

[a] Department of Physics, Faculty of Science and Technology, Optic Research Laboratory, Center of Excellence on Alternative Energy, Research and Development Institute, Sakon Nakhon Rajabhat University, 47000 Sakon Nakhon, Thailand
[b] Department of Chemistry—Ångström-Laboratory, Physical Chemistry, Box 523, Uppsala University, SE-751 20 Uppsala, Sweden
[c] Catalan Institute of Nanoscience and Nanotechnology (ICN2), CSIC and the Barcelona Institute of Science and Technology (BIST), Building ICN2, Campus UAB, E-08193 Bellaterra, Barcelona, Spain
[d] Department of Physics, Faculty of Science,Vali-e-Asr University of Rafsanjan, Rafsanjan 77139-36417, Iran

ARTICLE INFO

Keywords:
Carbon-based perovskite solar cells (C-PSCs)
SnO_2
Hexyl trimethylammonium bromide (HTAB)
Surface passivation
Carbon electrode

ABSTRACT

Low temperature processed carbon-based perovskite solar cells (C-PSCs) have gained great interest because of low cost and ease of fabrication. By replacing the Au electrode with carbon, stable solar cells suited for mass-production process can be made. However, power conversion efficiencies (*PCEs*) of C–PSCs still lag behind that of PSCs with Au contact.

Here we explore low temperature (≤150 °C) processed C-PSCs with, where a two-step method is used to prepare mixed-ion lead perovskite films, with tin oxide (SnO_2) electron transport layer, poly(3-hexylthiophene-2,5-diyl) (P3HT) hole transport layer and carbon electrode, resulting in devices with a *PCE* of 14.0%. Moreover, hexyl trimethylammonium bromide (HTAB) was introduced to improve the interface between perovskite and P3HT. Perovskite grains were remarkably enlarged into micrometer-size and defects were reduced. As a result, a champion *PCE* of 16.1% was obtained, mainly due to enhanced fill factor from 0.67 to 0.73. The interface modification by HTAB molecule is an effective way to passivate the perovskite defects and facilitate the carrier transport at the perovskite/HTL interface. Unencapsulated devices showed excellent stability over 1500 h stored under ambient air (relative humidity ~ 50 ± 10%).

1. Introduction

Hybrid metal halide perovskite solar cells (PSCs) are highly interesting materials for photovoltaic energy research; Their power conversion efficiencies (*PCE*) have rocketed from 3.8% to 25.7% in recent years [1,2]. These impressive *PCEs* can be achieved due to their unique optoelectronic properties including tunable bandgap, high absorption coefficient (~10^5 cm^{-1}), long charge carrier diffusion length (1>μm), low exciton-binding energies (~20 meV) and high defect tolerance [3–5]. The device stability is, however, far from ideal and may limit further industrial and practical exploitation. Poor stability arises from several components: The perovskite itself is water-sensitive and can degrade in the presence of light, and elevated temperature REF. The most commonly used hole transport material (HTM), 2,20,7,70- tetrakis-(N, N-di-4-methoxyphenylamino)−9,90-spirobifluorene (spiroOMeTAD) requires additional dopants, such as 4-tert-butylpyridine (t-BP), the hygroscopic bis(trifluoromethane)sulfonimide lithium salt (Li-TFSI) and tris (2-(1H-pyrazol-1-yl)−4-tert-butylpyridine)-cobalt(III)tris(bis-(trifluoromethylsulfonyl)imide)) (FK209), which lowers the device stability [6,7]. Noble metals contact such as gold (Au) or silver (Ag) are deteriorating the device stability due to migration of both halide ions and metal ions [8]. Therefore, metal contact are not suited for mass-produced PSC, also because of the relatively high cost and energy consumption of the thermal vacuum evaporation process [9].

To solve the drawback of these issues, various types of carbon electrodes (CEs) such as carbon black, graphene, graphite and carbon nanotubes (CNTs) have been applied in perovskite solar cells. These tend to be hydrophobic and can protect the perovskite layer from moisture corrosion, improving long term stability, thus contributing to large scale fabrication [10,11]. Furthermore, they have a suitable work function of

* Corresponding author.
E-mail address: gerrit.boschloo@kemi.uu.se (G. Boschloo).

https://doi.org/10.1016/j.electacta.2023.141935
Received 7 July 2022; Received in revised form 18 January 2023; Accepted 22 January 2023
Available online 23 January 2023

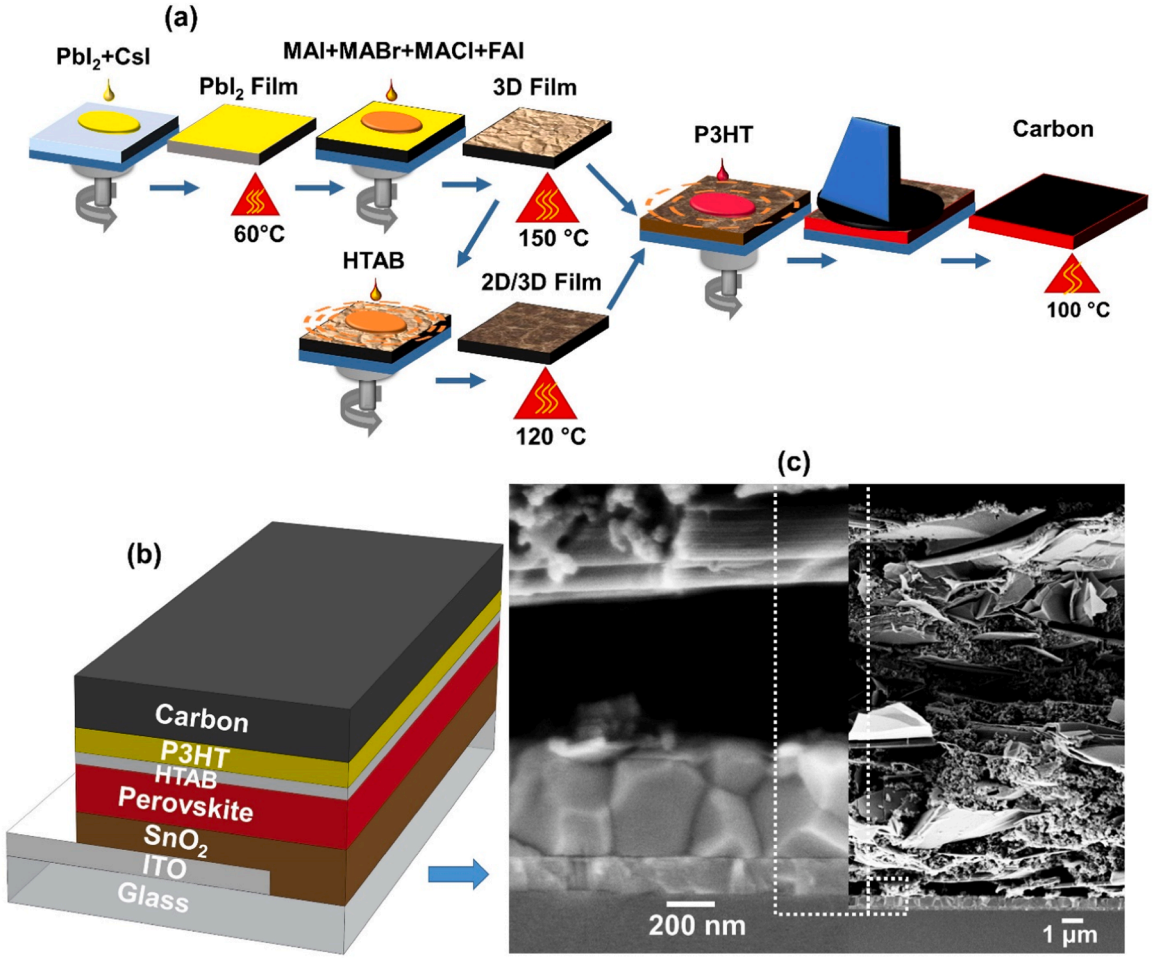

Fig. 1. Schematic diagram of (a) fabrication process (b) architecture of the HTAB passivated C-PSC (c) The cross–section SEM images of HTAB passivated C–PSCs, zoomed in on the perovskite layer (left) and complete cross section (right).

5.0 eV, low cost and can be deposited using vacuum-free printing techniques [12]. Carbon based perovskite solar cells (C-PSC) were first explored without hole transport layer (HTL) in a multi-layer mesoporous structure [13]. A typical multi–layer structure is composed of screen-printed layers of TiO_2, ZrO_2 and graphite / carbon black mixture, which are annealed at high temperature. Subsequently, perovskite solution is drop casted on the carbon surface to infiltrate through the mesoporous layers, which yielded a *PCE* from 6.6% [13] to 17.5% [14]. Both metal oxide and carbon layer typically require a high temperature ($\geq$ 450 °C) sintering step which increases the production costs and limits their applicability on flexible, polymeric substrates, and multi–junction device structures [15,16]. In contrast, SnO_2 electron transport layers (ETLs) are more attractive in PSCs compared with the traditional TiO_2, due to high performance and a low temperature deposition process ($\leq$150 °C), good stability and optical transparency, all desirable for commercial application [17,18]. The low-cost polymeric hole conductor poly (3-hexylthiophene-2,5-diyl) is a promising candidate for C-PSCs. Chu et al. investigated graphene-doped P3HT as HTM, delivering *PCE* from 11.1% to 17.8%, which was achieved due to the increase hole mobility from 8.3×10^{-3} to 1.2×10^{-2} cm^2 V^{-1} s^{-1} [19]. Undoped P3HT used in C-PSCs yielded a *PCE* of 15.7%, and maintained 70% of initial efficiency at 82 °C for 900 h in air [20].

Doping-free P3HT based n–i–p PSCs usually exhibit loss of open -circuit potential (V_{OC}) due to non-radiative recombination, lower carrier lifetime, and mismatched energy alignment at interface [21–23]. Fan et al. reported the dopant-free π- conjugated polymer PBDT(*S*)-T1 incorporated with 1,8-diiodooctane (DIO) that showed a *PCE* of 14.82% due to interface modification leading to enhanced charge transfer and defect passivation in C-PSC [24]. Recently, Zou et al. added 2,3,5,6-tetrafluoro-7,7,8,8- tetracyanoquinodimethane (F4TCNQ) into the perovskite of an undoped P3HT/carbon device, improving the *PCE* to 15.1% [25].

In perovskite solar cells, a high density of defect occurs in the bulk and at the grain boundaries of the polycrystalline perovskite film, which inevitably deteriorate the device performance. Hence, the defect healing is an effective way to reduce recombination and energy losses at the interfaces. This can be achieved by surface modification using long-chain alkyl or aromatic ammonium ions [26].

Various passivation strategies are developed to improve charge carrier extraction, suppress non-radiative recombination through the undesired grain boundaries leading to both high efficiency and stable PSCs [27,28]. Powerful passivation agents include phenylethylammonium iodide (PEAI), while methylammonium chloride (MACl) can significantly improve the perovskite crystallinity, enlarge crystal grain, reduce trap state, negligible hysteresis and long-term stability [29–32]. To eliminate the interface defects, halides passivators, such as adamantylammonium halides (ADAHX, X = Cl^-,Br^-,I^-) [33], cetyl trimethyl ammonium bromide (CTAB) [34] were investigated to reduce non-radiative recombination while ammonium group also could insert the cationic vacancies of the 3D perovskite which provided the resilience from moisture attack. To date, a high *PCE* of 24.6% was impressively achieved when n-hexyl trimethylammonium bromide (HTAB) was inserted between perovskite and P3HT after gallium (III) acetylacetonate ($Ga(acac)_3$) was directly incorporated into the

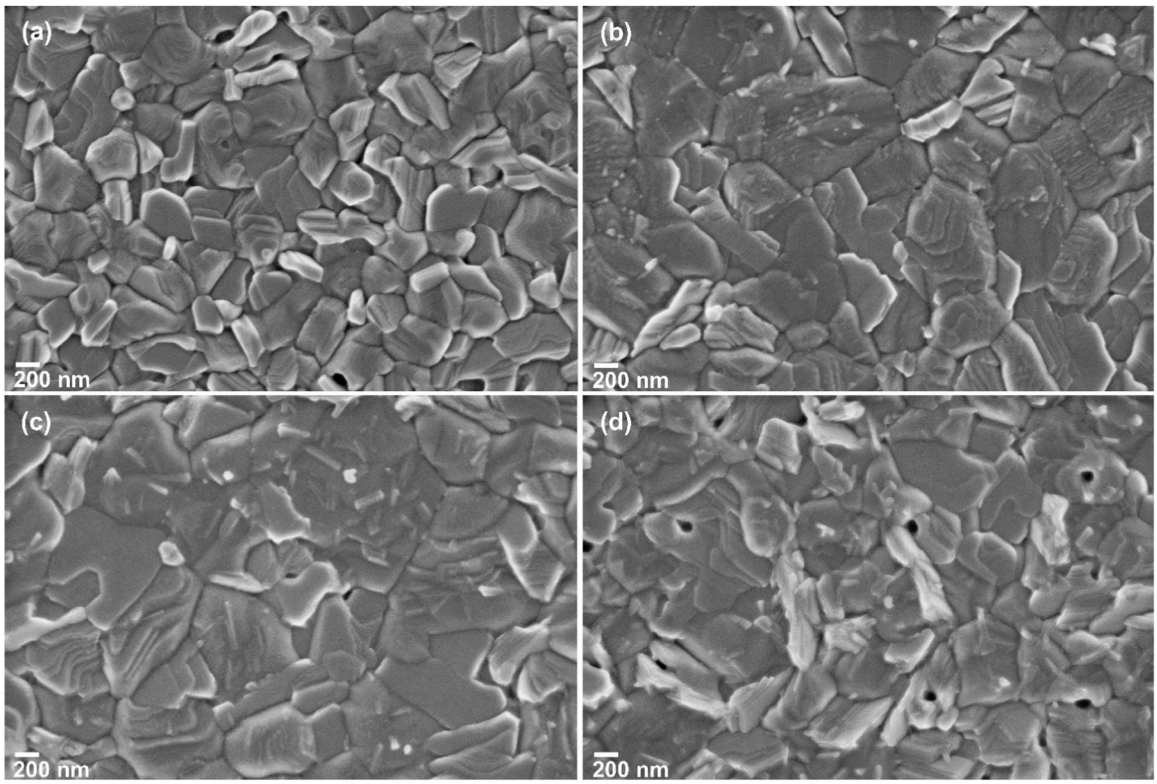

Fig. 2. SEM images of the pristine perovskite films with and without HTAB treatment of different molar concentration (a) 0 mM (b)1 mM (c) 2 mM (d) 3 mM at 200 nm scale bars.

HTL [35].

Lee et al. introduced the dual protection of two-dimensional (2D) perovskite layer (PEAI) to be good interface between perovskite and carbon electrode, suppressed the ion migration, improved efficiency up to 15.6%. Lewis-bases approaches in multiple ligand passivators create the stronger anchoring effects than monodentate coordination bonds, cationic and anionic vacancies which are passivated at the perovskite surface owing to more heteroatoms [36,37]. Recently, both pyridine and amino group, a bidentate passivator, 2-amino-5-(trifluoromethyl)pyridine (5-TFMAP) was applied to be stronger bonding between the metal-ligand complex and carbon electrode, enhanced efficiency up to 14.96% [38].

In this work, we report on low temperature processed C-PSC with interface modification using HTAB. Passivation effect on perovskite layer was effectively improved the crystallinity and enlarge grain sizes, attributed to the more efficient charge transfer, reduced recombination at perovskite/P3HT interface, resulting in drastically raised fill factor (*FF*) from 67% to 73% as well as reduced hysteresis from 8.7% to 3.4%. The *PCE* of a champion passivated device was boosted to 16.1% from 14.0% for reference devices. Storage of the devices, with and without HTAB, did not significantly reduce their performance, both in dry (relative humidity (RH) ~20 ± 5%) and ambient air (RH ~50 ± 10%).

2. Results and discussion

Mixed cation and halide perovskite films with an approximate composition ($Cs_{0.05}$ $FA_{0.54}MA_{0.41}$) $Pb(I_{0.98}$ $Br_{0.02})_3$, where FA and MA stand for formamidinium and methylammonium, respectively, are prepared by a two-step method, [23] followed by surface modification with HTAB forming an ultrathin 2D perovskite layer [22] (Fig. 1a). The positively charged trimethylammonium group from the HTAB can replace A-site cations at the perovskite surface or fill A-site vacancies there. The whole schematic structure of planar–type C-PSC is displayed in Fig. 1b. ETL for SnO_2 layer, perovskite absorber layer with and

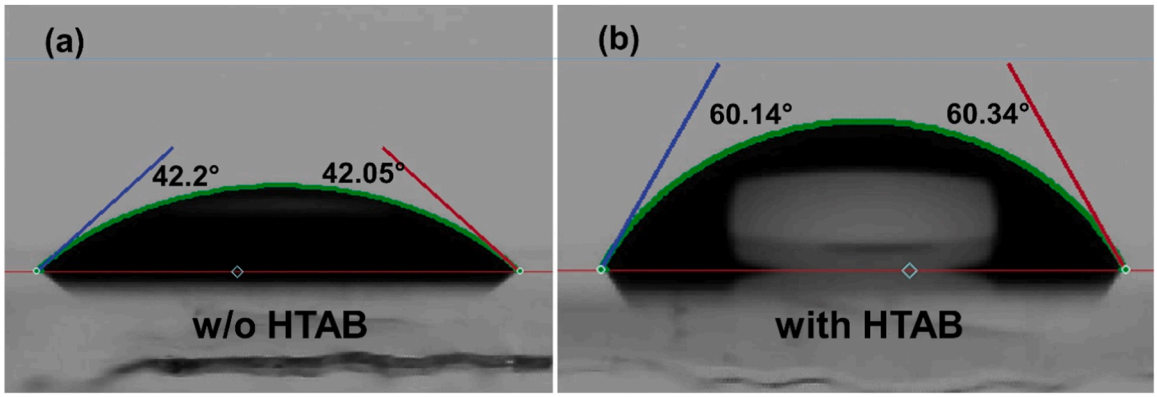

Fig. 3. Water contact angle measurement of perovskite films without HTAB (a) and with HTAB treatment (b).

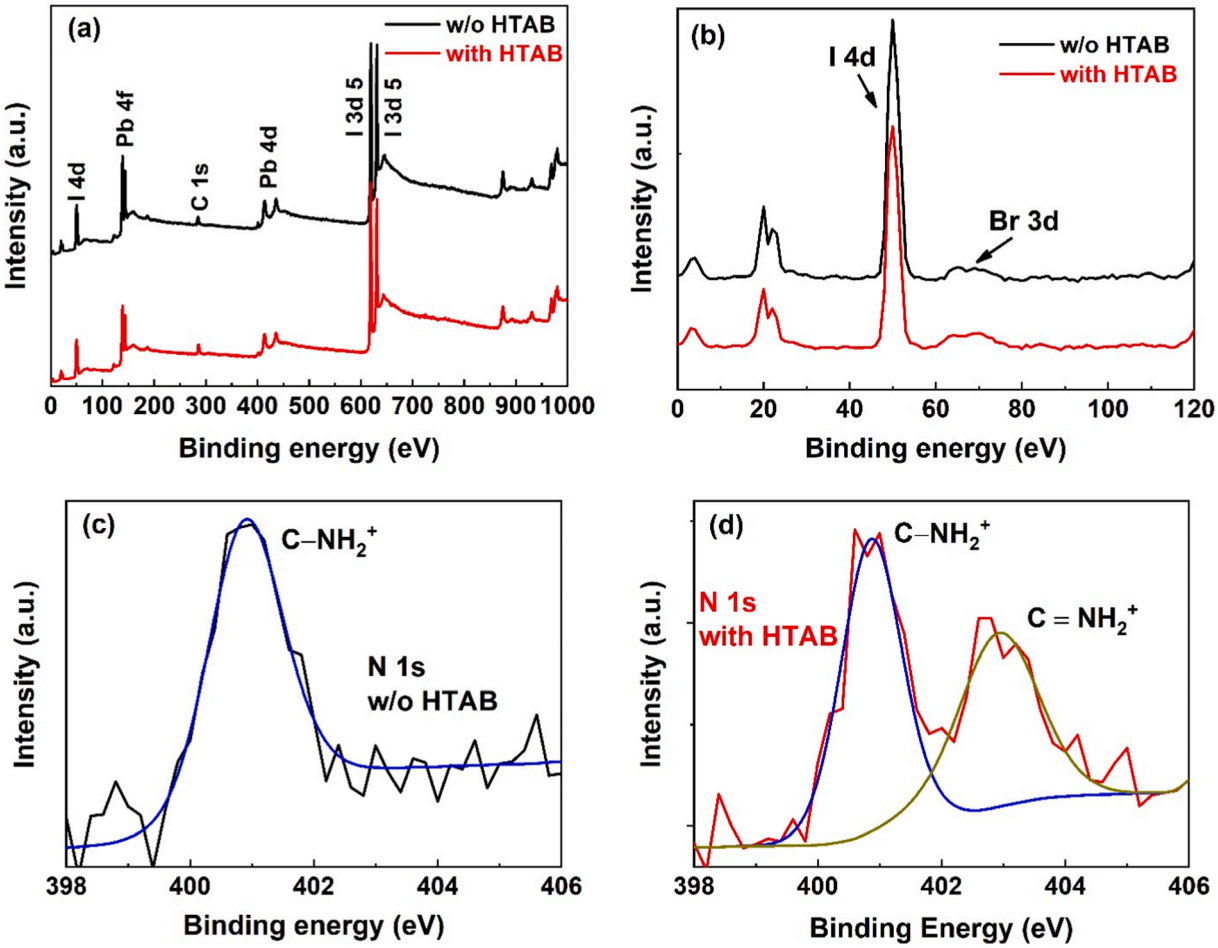

Fig. 4. (a) XPS survey spectra with and w/o HTAB modification films. (b) I/Br core level XPS spectra of mixed perovskite with and w/o HTAB modified films. XPS core-level spectra of N 1 s of (c) pristine and (d) passivated perovskite films.

without (w/o) HTAB modification, P3HT as doping–free hole conductor was processed by spin–coated method. Finally, carbon paste was deposited on the P3HT using doctor blading. The cross-sectional scanning electron microscopy (SEM) images of C-PSC (see Fig. 1c) demonstrate that the carbon layer is about 20 μm thick and contains large flakes of graphite. The magnified view show that large grains of perovskite films are neatly arranged to the normal direction; the thickness is about 470 nm.

Top view of SEM image of perovskite surfaces with and without HTAB are shown in Fig. 2. The pristine film shows some unreacted PbI_2 white grains and several pin–holes. After HTAB treatment (1 and 2 mM), full coverage, compact and dense morphologies are obtained, presumably due to reaction of PbI_2, as well as some of the 3D perovskite, with HTAB to form a 2D perovskite layer on top of the 3D perovskite surface. As a result, the maximum grain size of pristine film (~880 nm), is significantly increased up to 1.5 μm. For 3 mM HTAB treatment more pin–holes are evident in the SEM top-view.

Fig. 3 illustrates the water contact angle tests on untreated and HTAB-treated films to further confirm the presence of the amphiphilic HTAB molecule. The HTAB-treated perovskite films show an average contact angle of 60.24°, which is higher than pure perovskite film which has an average contact angle of 42.13° This can be directly related to the apolar nature of the hexyl chains from the HTAB that point upward [39].

XRD analysis shows that the perovskite peaks at 14.1° (110) and 28.47° (220) are remarkably increased due to HTAB modification, which suggests enhanced crystallization of perovskite film (supporting information, Fig. S1). There is a significant PbI_2 peak at 12.7° remaining in the film, which is a rather common feature in the 2-step method as used here. The peak is, however, lower in HTAB-treated films than in pristine films.

To understand the elementary composition on the passivated films, survey and core-level X-ray photoelectron spectroscopy (XPS) spectra of perovskite films with and w/o HTAB are displayed in Fig. 4a. A change in the I/Br ratio is confirms addition of Br from HTAB molecules (Fig. 4b). The I/Br atomic ratio decreased from 4.60 to 3.94 in HTAB-modified perovskite films [40]. Fitting results can be seen in supporting information, Fig. S2. The N 1 s spectrum for films without HTAB display only one peak at 400.9 eV(Fig. 4c), which can be attributed to nitrogen in FA [40]. No clear evidence for MA is found, which should give a peak for N at 402.5 eV. Upon HTAB treatment, a clear peak at 402.9 eV appears, which is attributed to the nitrogen in HTAB (Fig. 4d). In addition, Fig. S4 shows no distinct shift peaks are observed at the spin-orbit splitting of Pb $4f_{7/2}$, Pb $4f_{5/2}$ (~139.6, ~143.5 eV) and I $3d_{5/2}$ and $3d_{3/2}$ (~619.5, ~631 eV) [23,41]. Compared with the pristine film, the atomic ratio of I/Pb is slightly increased from 2.63 to 2.89 after the treatment of HTAB. Thus, the elemental analysis of (*I*+ Br3d)/Pb ratios of pristine and HTAB treated film are 2.75 and 3.07 while (I + C1s)/Pb ratios are 2.70 in the original film and 3.04 in the modified film, respectively (see Table S1 and S2).

Furthermore, HTAB modified perovskite film was determined by energy-dispersive X-ray spectroscopy (EDS), see Fig. S5. From the elemental mapping it is evident that the Br signal from the HTAB is uniformly distributed on the surface area of the film. For this purpose a pure $FAPbI_3$ films was used.

Fig. S6 shows the Raman spectra of perovskite films with and w/o HTAB modification. The perovskite peak at 137 cm^{-1} increased in

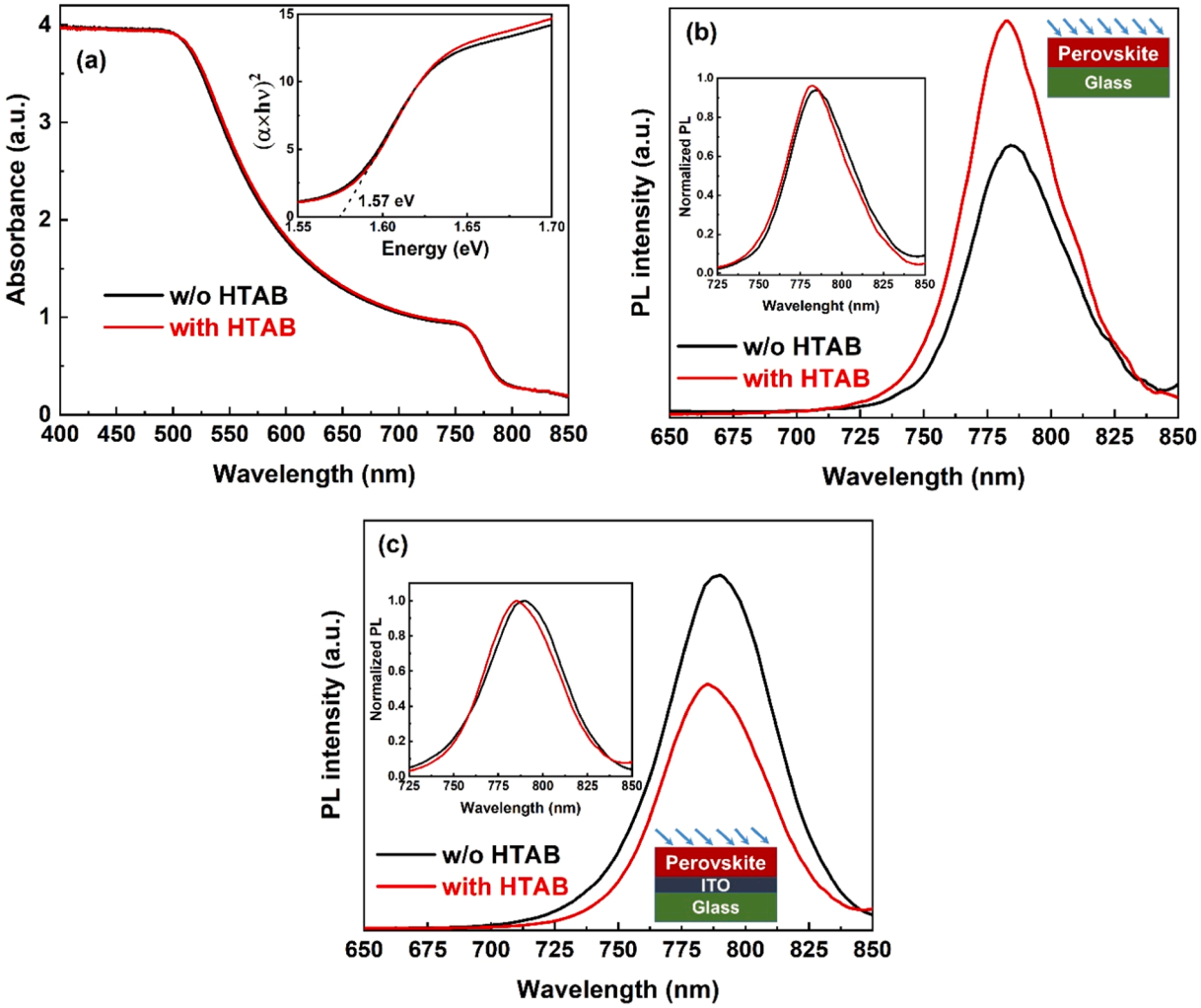

Fig. 5. (a) UV–Vis absorption spectra of different perovskite films, 1.57 eV estimated from the Tauc plot. Steady-state PL spectra of films with and w/o HTAB, excitation wavelength 470 nm (b) on the perovskite/glass substrate (c) on the perovskite/ITO/glass substrate.

magnitude and shifted to higher frequency values (141 cm^{-1}) upon HTAB modification. This suggests improved film crystallization and due to interaction between HTAB and the perovskite surface. Moreover, the appearance of PL background indicated the successful passivation of surface traps by HTAB.

The optical properties of untreated and HTAB-treated films have been studied by UV–Vis. The onset of absorbance spectra is nearly identical around 780 nm in Fig. 5a. The optical absorption of HTAB-

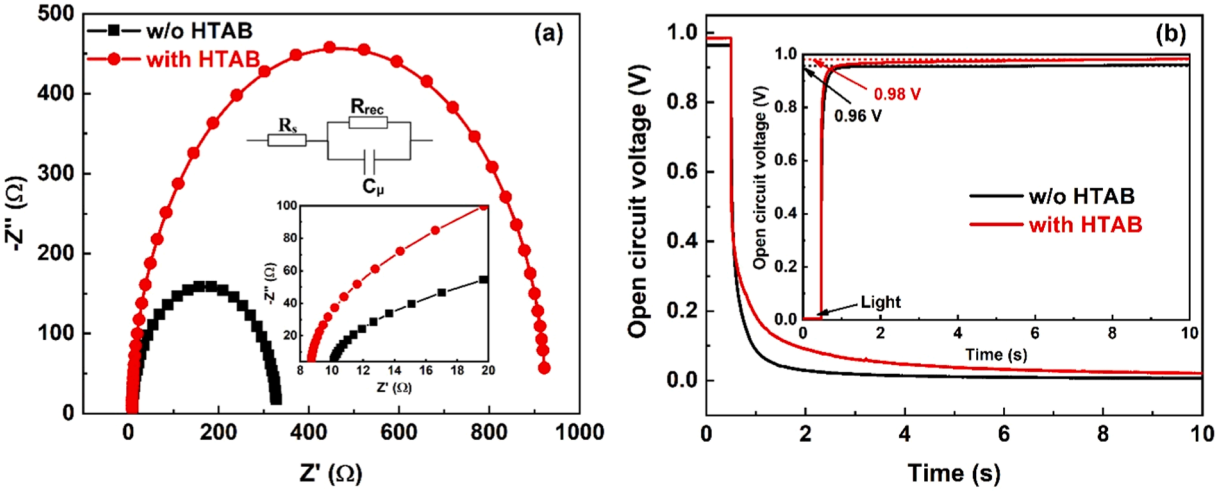

Fig. 6. (a) Nyquist plot of pristine and HTAB-passivated devices measured at 0.90 V under the dark. (b) V_{oc} decay measurement. Inset shows stabilized open circuit voltage of each type.

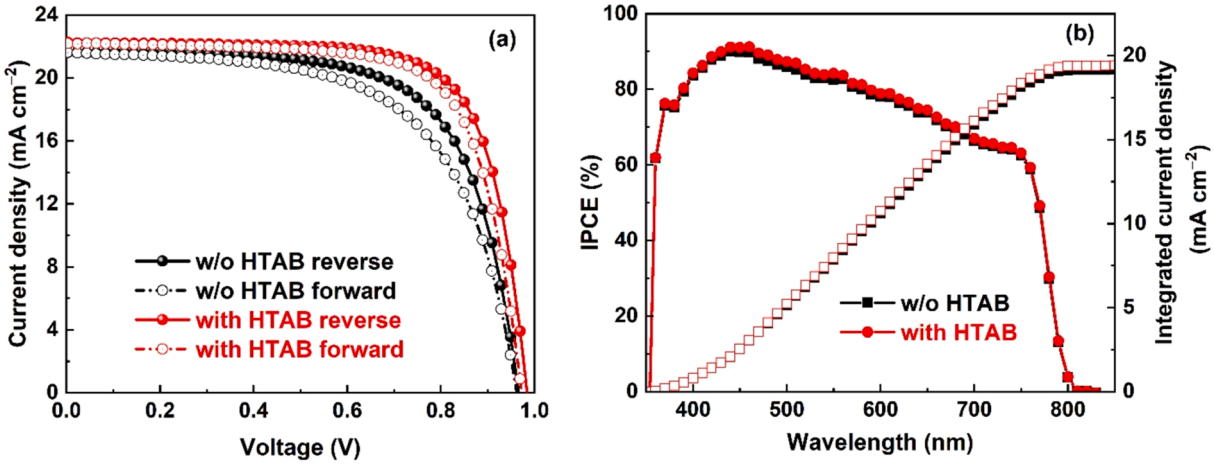

Fig. 7. (a) Hysteresis J–V curves of champion devices of pristine and HTAB-treated devices. (b) IPCE spectra with integrated J_{SC} derived from IPCE spectra over the standard AM 1.5 G.

treated film was slightly higher in the visible range (see inset Fig. 5a). The HTAB treatment film did not affected the optical bandgap (E_g) of about 1.57 eV calculated from Tauc-plot (Fig. 5a inset).

To study recombination in untreated and HTAB-treated films, steady-state photoluminescence (PL) analysis was performed. The steady-state PL intensity is clearly increased for passivated perovskite films on glass substrate, indicating reduced non-radiative recombination (see Fig. 5b). In Fig. 5c, stronger PL quenching of passivated film is observed when it is deposited on the ITO substrate. This suggests improved electron transfer to the ITO substrate, as a result of the passivation, which is slightly unexpected since HTAB treatment should mostly affect the perovskite / air interface [38]. It is found that PL peak slightly shifts to shorter wavelengths from 789 nm to 785 owing to passivation effects, see inserts in Fig. 5b,c [42].

To further probe the effect of HTAB treatment, electrochemical impedance spectroscopy (EIS) was investigated at applied forward bias of 0.90 V under the dark. The Nyquist plot in the frequency range is set from 500 kHz to 1 Hz with a complete semicircle. The equivalent circuit model and fitted parameters extracted from the EIS spectra are shown in Fig. 6a and Table S3. The high frequency intercept in the Nyquist plot gives the series resistance (R_s) of the device, which originates from the resistance of the ITO and the carbon electrode. The inset shows that R_s amount to about 9 Ω for both types of devices. The semicircle is given by the geometric capacitance (C_{geom}) and the recombination resistance (R_{rec}) of the system [43]. HTAB treatment in perovskite device leads to an increase of R_{rec} from 318 Ω to 917 Ω, indicating slower charge recombination kinetics at the perovskite/P3HT/carbon interface. The carrier lifetime (τ_e) of pristine and passivated devices were 18.4 μs and 57.4 μs, respectively, calculated by this equation: $\tau_e = R_{rec}\ C_{geom}$. Increased carrier lifetime attributed to the reduced recombination at P3HT/carbon interface, improving device performance due to higher *FF* and *PCE*. These results are in good agreement with the *J–V* curves and V_{OC} decay.

A slight improvement of V_{OC} is found upon HTAB modification. To validate the V_{OC} enhancement, steady-state open circuit voltage (V_{OC}) traces were monitored under 1 sun illumination [44]. The stabilized V_{OC} for the passivated device showed higher value of 0.98 V compared with the pristine device of 0.96 V (inset Fig. 6b). Furthermore, steady–state V_{OC} under 1 sun for devices without MAI was stabilized to 0.95 V (without HTAB) and 0.99 V (with HTAB), as displayed in Fig. S7. V_{OC} decay measurements displayed a marked difference for devices with or without HTAB modification, see Fig. 6b. After initial fast decay for both, the V_{OC} in HTAB devices decayed slower in the second part, which might be related to the slow release of ions accumulated at interfaces.

Fig. 7a shows the *J–V* curves of C-PSCs in forward and reverse scans.

Table 1
The key photovoltaic parameters derived from ***J–V*** curves of champion and average devices.

Devices	Scan	***PCE*** (%)	V_{oc} (V)	***FF*** (%)	J_{sc} (mA cm^{-2})	***HI***
w/o HTAB	Reverse	14.04	0.966	67.16	21.64	0.087
	Forward	12.82	0.963	61.60	21.61	
Average	Reverse	13.35 ±0.47	0.93 ±0.018	65.34 ±1.61	21.89 ±0.23	0.10 ±0.058
With HTAB	Reverse	16.08	0.984	73.48	22.23	0.034
	Forward	15.53	0.973	71.83	22.22	
Average	Reverse	15.25 ±0.64	0.97 ±0.016	69.43 ±2.48	22.68 ±0.36	0.056 ±0.028

A champion *PCE* of 16.08% is achieved using modification by HTAB, leading to a remarkable increase in *FF* up to 73.48%, J_{SC} up to of 22.23 mA cm^{-2} and a V_{OC} of 0.984 V. In contrast, the pristine device achieves a champion *PCE* of 14.04%, a J_{SC} of 21.64 mA cm^{-2}, a V_{OC} of 0.966 V and a *FF* of 67%. Variation of the concentration of HTAB from 1 mM to 2 mM in isopropanol yielded similar average *PCEs* (~15.3%) in C-PSCs (see Figure S8 and Table S4). The statistical distribution of 2 mM HTAB concentration on the photovoltaics parameters for 10 devices can be seen in Fig. S9.

Hysteresis in *J–V* curves was significantly reduced in the HTAB-modified C-PSC devices. The hysteresis index (*HI*) index was calculated from forward and reverse scans by the following formula [45]:

$$HI = \frac{PCE_{reverse} - PCE_{forward}}{PCE_{reverse}} \quad (1)$$

HI of champion devices is effectively reduced from 8.7% (w/o HTAB) to 3.4% (with HTAB) device. Moreover, the average modified *HI* values (0.056 ± 0.028) are effectively lower than that of pristine (0.10 ± 0.058) values. These results are summarized in Table 1.

The incident photon to current efficiency (*IPCE*) spectra of C-PSCs showed values over 80% in the wavelength of 400–600 nm as shown in Fig. 7b. The integrated J_{SC} with HTAB device (19.39 mA cm^{-2}) was slightly higher than that of 3D device (19.14 mA cm^{-2}), while corresponding measured values from *J–V* curves for pristine and modified device are 22.34 mA cm^{-2} and 22.57 mA cm^{-2}; We ascribe the lower values of integrated J_{SC} due to the very low light intensity of monochromatic light used in IPCE measurements. The trend in integrated J_{SC} value is comparable to that of J_{SC} value from *J–V* curves.

To validate the reproducibility of photovoltaic (PV) cells, statistical distribution of (2 × 17 cells) pristine and HTAB-modified devices are given in Fig. 8. The average *PCEs* (15.25 ± 0.64%) of passivated devices

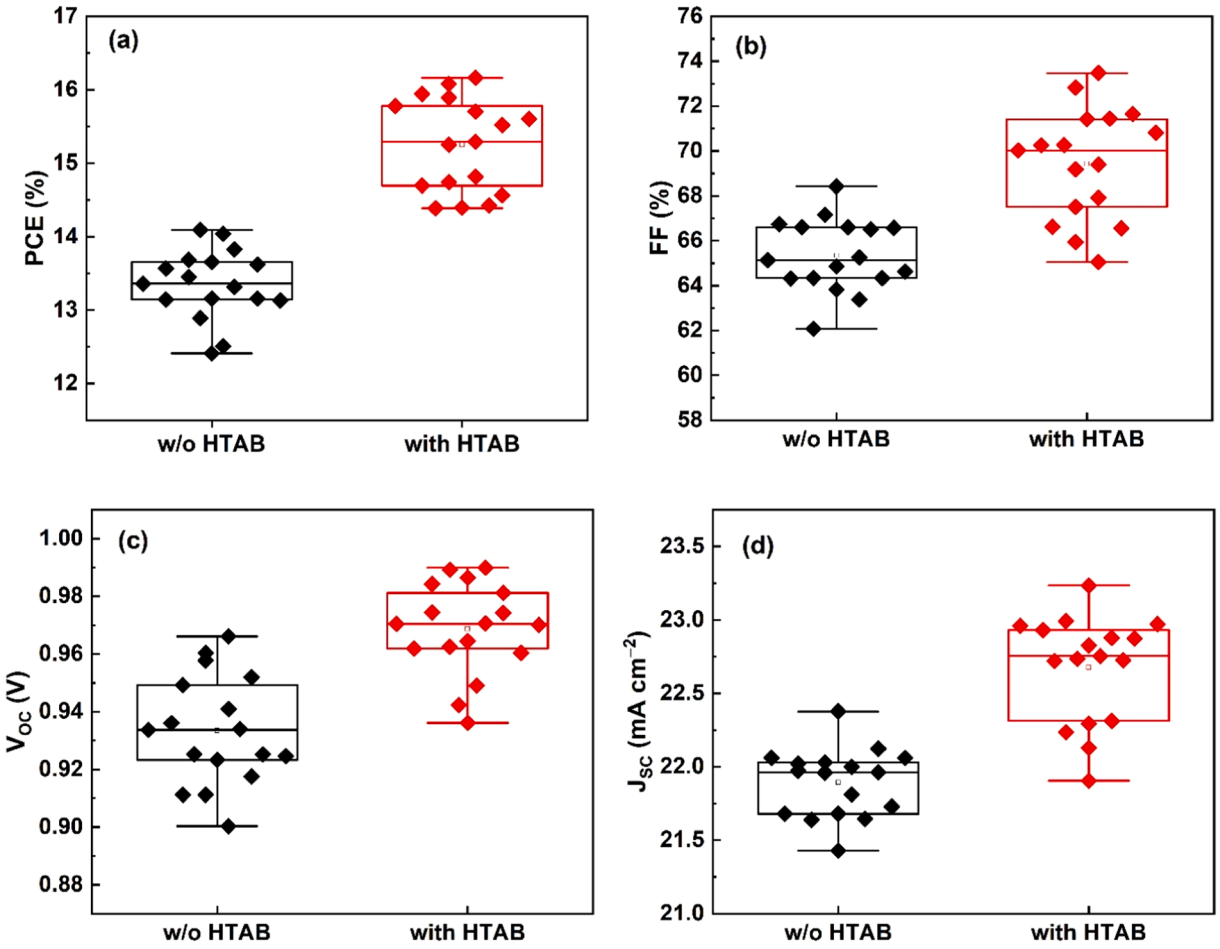

Fig. 8. Statistical analysis results obtained from 17 cells of each pristine and 1 mM HTAB-modified devices for (a) *PCE* (b) *FF* (c) V_{OC} and (d) J_{SC}. All characterization is carried out under 1 sun illumination (AM 1.5 G) at room temperature with an active area of 0.125 cm^2.

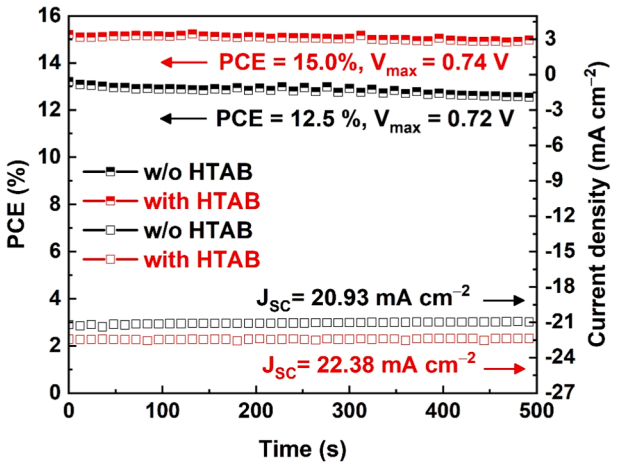

Fig. 9. Stabilized power out measured by maximum power point tracking for 500 s for un–capsulated devices in ambient air.

are significantly higher than that of pristine devices, owing to improvement of average *FF* (69.43 ± 2.48%), V_{OC} (0.97 ± 0.016 V) and J_{SC} (22.68 ± 0.36 mA cm^{-2}) listed in Table 1. In the unmodified devices, the average *PCE* was 13.35 ± 0.47% and all other solar cells parameters were slightly lower too.

Similar trends were found for devices prepared without MAI in the second step of perovskite film preparation. These C–PSCs exhibited a maximum *PCE* of 13.7% for pristine and 14.79% for HTAB-modified devices (Fig. S10, Table S5), with much lower *HI* upon HTAB-modification. In addition, the statistical distributions show that *PCE* and V_{OC} are significantly improved by HTAB modification (Fig. S11).

To assess reliability of C-PSCs, steady state power output, devices with and without HTAB were tested by maximum power point tracking (MPPT) as shown in Fig. 9. The HTAB-modified device exhibits a stabilized *PCE* of 15.0% and current density of 22.38 mA cm^{-2} with a maximum power point at V_{max} of 0.74 V while *PCE* of pristine device decreased to 12.5% after illumination for 500 s, with a current density of 20.93 mA cm^{-2} (V_{max} = 0.72 V). The stabilized efficiency of the HTAB-modified C-PSC was close to the 15.25% measured from reverse *J-V* scan. Furthermore, steady-state *PCEs* were measured for 50 min under 1 sun illumination. Stabilized *PCEs* of 12.06% (pristine) and 14.35% (passivated) devices were observed under MPPT after 50 min (see Fig. S12).

Currently, long-term stability is one of the key challenges for perovskite solar cells. Hence, the stability test was performed for unencapsulated C-PSC devices stored in the dark in dry air (RH ~ 20 ± 5%) or ambient air (RH ~50 ± 10%) at room temperature. No obvious efficiency drop was observed during 1500 h storage (see in Fig. 10). The HTAB device in air displayed an enhancement of efficiency due to improvement in *FF* and J_{SC} (Fig. S13).

In addition, when the passivated device is kept in dry air for 1752 h, V_{OC} is increased from 0.97 to 1.02 V with a slight lower current density (from 22.71 to 22.01 mA cm^{-2}) and fill factor (from 70.83% to 68.52%). However, stabilized efficiency (~15.5%) of these devices is preserved (see Fig. S14). It is noted that co-solvents in the carbon electrode may

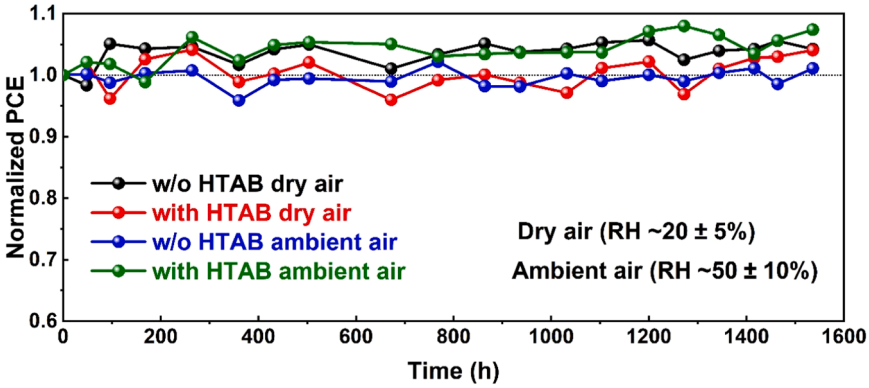

Fig. 10. Dark storage stability tests without encapsulated devices under dry condition (RH ~20 ± 5%) and ambient air (RH ~50 ± 10%).

gradually evaporate without any damage or degradation of perovskite layer during stored in the dry air. The improved interface between perovskite and P3HT/carbon causes the enhanced *Voc*.

Thermal stress testing at 82 °C in air for unencapsulated C-PSC devices showed moderate stability in this study, see Fig. S15. Devices showed a gradual decrease and 70% of the initial *PCE* was retained after 310 h. We believe that remaining PbI_2 in the perovskite films (prepared using a two-step method) is responsible for relatively poor thermal stability, because in our previous work using C-PSC with $MAPbI_3$ (one-step method), 70% of the PCE was maintained after 900 h [20].

3. Conclusions

Hexyl trimethylammonium bromide treatment of mixed-ion perovskite films significantly improves the performance of perovskite solar cells with P3HT as hole conductor and a carbon contact. This treatment modifies the perovskite surface, leading to increased grain size and reduced non-radiative recombination at the perovskite/P3HT interface, yielding higher open-circuit potentials and solar cell efficiencies. Importantly, the hysteresis in *J-V* curves is significantly reduced by the treatment. Unencapsulated devices showed excellent storage stability in ambient air, where no degradation was found during 1500 h.

4. Experimental section

4.1. Materials and solar cell preparation

Lead (II) iodide (PbI_2, 99.99%) and hexyl trimethylammonium bromide (HTAB, >98.0%) were purchased from TCI. Formamidinium iodide (FAI, >99.99%), methylammonium iodide (MAI > 99.99%), methylammonium bromide (MABr>99.99%) and methylammonium chloride (MACl >99.99%) were ordered from Greatcell Solar. Poly (3-hexylthiophene-2,5-diyl), (P3HT, regioregular, average M_w 50,000–100,000, prod. no. 445703, Sigma-Aldrich), cesium iodide (CsI, 99.99%, Sigma-Aldrich), 2-propanol anhydrous (IPA, 99.5%, Sigma-Aldrich), N,N-dimethylformamide (DMF, 99.8%, ACROS), methyl sulfoxide (DMSO, 99.7%, ACROS), chlorobenzene (CB, 99.8%, ACROS), carbon paste (Dyenamo, DN—CP01). Tin (IV) oxide, (SnO_2, 15% in H_2O colloidal dispersion) was purchased from Alfa Aesar. All purchased chemicals were used without further purification.

Indium tin oxide (ITO, 15 Ω/sq, Optical Filters, 2.4 × 2.8 cm^2) glass substrates were first etched using 2 M of hydrochloric (HCl) acid with deionized water (DI). And then, followed by sonication in sequence with 2% Hellmanex in water solution, DI, acetone and ethanol for 20 min each. The cleaned substrates were dried using a stream of air. Then, the patterned ITO was treated with ultraviolet ozone (UVO) for 30 min before deposition ETL. After that, colloidal SnO_2 solution was diluted with DI volume ratio of 4 to 1, then spin coated on the ITO substrate at 3000 rpm for 30 s. Then, all substrates were heated at 150 °C for 30 min in ambient air. After having cooled down to room temperature (RT), they were cleaned by UVO again before use. The perovskite precursor solution was prepared by two-step spin coating method [23]. At first, 1.3 M PbI_2 additive with 5% CsI solution was dissolved in solvent of DMF/DMSO (9:1 v/v). Then, PbI_2 solution was deposited on the ITO/SnO_2 layer at 2500 rpm for 30 s. Then, it was annealed at 60 °C for 60 s in the N_2 filled glove box. After cooling down, 0.12 M MAI, 0.05 M MABr, 0.07 M MACl and 0.23 M FAI mixed in the IPA solution was poured on the PbI_2 layer and spin–coated at 2300 rpm for 30 s. Then, it was taken out from the N_2 glovebox and annealed at 150 °C for 15 min in ambient air (RH ~50 ± 10%). For HTAB interlayer 2D devices, 1 mM of hexyl trimethylammonium bromide solution was diluted in IPA solvent and then spin–coated on perovskite layer at 3000 rpm for 30 s and followed by annealing at 120 °C for 60 s in the N_2 filled glove box. For a thin P3HT hole selective layer on all devices, 10 mg of P3HT in 1 mL of CB was spun coated at 3000 rpm for 30 s. Finally, carbon paste was coated on the P3HT layer using doctor blading method, and annealed at 100 °C for 20 min on a hotplate in ambient air.

4.2. Characterizations methods

The current density and voltage (*J–V*) measurements were performed using a Sinus-70 solar simulator (Wavelabs, Leipzig, Germany) in the ambient atmosphere under 1 sun illumination (AM 1.5 G) at room temperature. A black metal mask with a circular aperture of 0.125 cm^2 was used to define the active area. Reverse (from 1.05 to –0.1 V) and forward scans (from –0.1 to 1.05 V) in all devices were set to a scan speed of 50 mV/s. Storage stability tests of unencapsulated devices was done in the dark in a dry box (relative humidity, RH ~20 ± 5%) or in ambient air (RH ~ 40 ± 10%). IPCE spectra were recorded with a xenon lamp (Spectral products ASB-XE-175), a monochromator (Spectral Products CM110) and a LabJack U6 digital acquisition board in the wavelength range from 350 nm to 850 nm. The light intensity was calibrated using a certified silicon photodiode (Fraunhofer ISE) prior to characterization. The ultraviolet−visible (UV−vis) spectra were measured using a Varian Cary 5000 spectrophotometer. The surface morphology and cross–sectional scanning electron microscopy (SEM) images of the samples were observed using the Zeiss LEO 1530/1550 microscope. The X-ray diffraction (XRD) patterns were obtained by a Siemens D5000 θ−2θ goniometer with Cu Kα (λ = 1.54051 Å) under ambient air condition. The steady state photoluminescence (PL) spectra were recorded on a HORIBA Jobin Yvon Fluorolog station, with excitation wavelength at 470 nm from the perovskite side. The samples were prepared by with and without HTAB treatment perovskite films onto the ITO glass substrates. Electrochemical impedance spectroscopy (EIS) of devices were examined by an Autolab Potentiostat/Galvanostat (PGSTA100) under the dark at an applied voltage (0.9 V). Fitting parameters were collected using FRA 4.5 (Frequency Response Analyzer) software to obtain from the frequency range between 500 kHz and 1 Hz

with an AC perturbation of 10 mV. Open–circuit voltage (V_{oc}) decay recorded using a homebuilt system with a white LED light (Luxeon Star 1 W) and digital acquisition board (National Instrument 6252). X-ray photoelectron spectra (XPS) were recorded by using a Physical Electronics Quantera II using AlKα (1486.6 eV) X-rays at a pressure below 7 × 10^{-9} Torr. The binding energy was calibrated against the Fermi level by measuring the Au4f core levels of a gold foil mounted on the manipulator and setting the binding energy of $Au4f_{7/2}$ to 84.0 eV. XPS data analysis was carried out with CasaXPS (H243 UU Site License) software.

CRediT authorship contribution statement

S.K.K.A., T.S. and G.B.: devised the research. **S.K.K.A.** performed all experiment unless noted otherwise. **A.V.** performed SEM, XRD, PL and UV–vis spectroscopy. **M. K.** performed and analyzed XPS, EDS and Raman experiments. **S.K.K.A. and G.B.** wrote the manuscript. **G.B.** supervised the work.

Declaration of Competing Interest

The authors declare that they have no known competing financial interests or personal relationships that could have appeared to influence the work reported in this paper.

Data availability

Data will be made available on request.

Acknowledgement

This work was financially supported from Thailand International Cooperation Agency (TICA), Thailand Science Research and Innovation (TSRI), National Research Council of Thailand (NRCT) from The Royal Golden Jubilee (RGJ) Programme, Swedish International Development Cooperation Agency (Sida) and International Science Program (ISP) at Uppsala University under Thai-Swedish Trilateral Development Cooperation Programme (grant no. PHD/0101/2560), the Swedish Foundation for Strategic Research (project no. RMA15–0130), and the Standup for Energy program for financial support. We thank Dr. Byeong-Jo Kim for useful discussions.

Supplementary materials

Supplementary material associated with this article can be found, in the online version, at doi:10.1016/j.electacta.2023.141935.

References

[1] A. Kojima, K. Teshima, Y. Shirai, T. Miyasaka, Organometal halide perovskites as visible-light sensitizers for photovoltaic cells, J. Am. Chem. Soc. 131 (2009) 6050–6051, https://doi.org/10.1021/ja809598r.
[2] NREL, Best Research-Cell Efficiency Chart, https://www.nrel.gov/pv/assets/pdfs/best-research-cell-efficiencies.pdf.
[3] B.W. Park, B. Philippe, S.M. Jain, X. Zhang, T. Edvinsson, H. Rensmo, B. Zietz, G. Boschloo, Chemical engineering of methylammonium lead iodide/bromide perovskites: tuning of opto-electronic properties and photovoltaic performance, J. Mater. Chem. A. 3 (2015) 21760–21771, https://doi.org/10.1039/c5ta05470b.
[4] F. Wang, S. Bai, W. Tress, A. Hagfeldt, F. Gao, Defects engineering for high-performance perovskite solar cells, Npj Flex. Electron. 2 (2018), https://doi.org/10.1038/s41528-018-0035-z.
[5] H.J. Eggimann, J.B. Patel, M.B. Johnston, L.M. Herz, Efficient energy transfer mitigates parasitic light absorption in molecular charge-extraction layers for perovskite solar cells, Nat. Commun. 11 (2020), https://doi.org/10.1038/s41467-020-19268-w.
[6] G. Ren, W. Han, Y. Deng, W. Wu, Z. Li, J. Guo, H. Bao, C. Liu, W. Guo, Strategies of modifying spiro-OMeTAD materials for perovskite solar cells: a review, J. Mater. Chem. A 9 (2021) 4589–4625, https://doi.org/10.1039/d0ta11564a.
[7] G. Tumen-Ulzii, T. Matsushima, C. Adachi, Mini-review on efficiency and stability of perovskite solar cells with spiro-OMeTAD hole transport layer: recent progress and perspectives, Energy Fuels 35 (2021) 18839–18844, https://doi.org/10.1021/acs.energyfuels.1c02190.
[8] K. Domanski, J.P. Correa-Baena, N. Mine, M.K. Nazeeruddin, A. Abate, M. Saliba, W. Tress, A. Hagfeldt, M. Grätzel, Not all that glitters is gold: metal-migration-induced degradation in perovskite solar cells, ACS Nano 10 (2016) 6306–6314, https://doi.org/10.1021/acsnano.6b02613.
[9] F. Zhang, X. Yang, H. Wang, M. Cheng, J. Zhao, L. Sun, Structure engineering of hole-conductor free perovskite-based solar cells with low-temperature-processed commercial carbon paste as cathode, ACS Appl. Mater. Interfaces 6 (2014) 16140–16146, https://doi.org/10.1021/am504175x.
[10] W. Chen, X. Yin, M. Que, H. Xie, J. Liu, C. Yang, Y. Guo, Y. Wu, W. Que, A comparative study of planar and mesoporous perovskite solar cells with printable carbon electrodes, J. Power Sources. 412 (2019) 118–124, https://doi.org/10.1016/j.jpowsour.2018.11.031.
[11] M. Que, B. Zhang, J. Chen, X. Yin, S. Yun, Carbon-based electrodes for perovskite solar cells, Mater. Adv. 2 (2021) 5560–5579, https://doi.org/10.1039/d1ma00352f.
[12] H. Zhang, K. Song, L. Zhu, Q. Meng, Back-interface regulation for carbon-based perovskite solar cells, Carbon N. Y. 168 (2020) 372–391, https://doi.org/10.1016/j.carbon.2020.06.065.
[13] A. Mei, X. Li, L. Liu, Z. Ku, T. Liu, Y. Rong, M. Xu, M. Hu, J. Chen, Y. Yang, M. Grätzel, H. Han, A hole-conductor-free, fully printable mesoscopic perovskite solar cell with high stability, Science 345 (80) (2014) 295–298, https://doi.org/10.1126/science.1254763.
[14] X. Chen, Y. Xia, Q. Huang, Z. Li, A. Mei, Y. Hu, T. Wang, R. Cheacharoen, Y. Rong, H. Han, Tailoring the dimensionality of hybrid perovskites in mesoporous carbon electrodes for type-II band alignment and enhanced performance of printable hole-conductor-free perovskite solar cells, Adv. Energy Mater. 11 (2021), 2100292, https://doi.org/10.1002/aenm.202100292.
[15] H. Zhou, Y. Shi, K. Wang, Q. Dong, X. Bai, Y. Xing, Y. Du, T. Ma, Low-temperature processed and carbon-based ZnO/CH3NH3PbI3/C planar heterojunction perovskite solar cells, J. Phys. Chem. C. 119 (2015) 4600–4605, https://doi.org/10.1021/jp512101d.
[16] G. Yang, H. Tao, P. Qin, W. Ke, G. Fang, Recent progress in electron transport layers for efficient perovskite solar cells, J. Mater. Chem. A. 4 (2016) 3970–3990, https://doi.org/10.1039/c5ta09011c.
[17] L. Xiong, Y. Guo, J. Wen, H. Liu, G. Yang, P. Qin, G. Fang, Review on the application of SnO2 in perovskite solar cells, Adv. Funct. Mater. 28 (2018), 1802757, https://doi.org/10.1002/adfm.201802757.
[18] C. Altinkaya, E. Aydin, E. Ugur, F.H. Isikgor, A.S. Subbiah, M. De Bastiani, J. Liu, A. Babayigit, T.G. Allen, F. Laquai, A. Yildiz, S. De Wolf, Tin oxide electron-selective layers for efficient, stable, and scalable perovskite solar cells, Adv. Mater. 33 (2021), 2005504, https://doi.org/10.1002/adma.202005504.
[19] Q.Q. Chu, B. Ding, J. Peng, H. Shen, X. Li, Y. Liu, C.X. Li, C.J. Li, G.J. Yang, T. P. White, K.R. Catchpole, Highly stable carbon-based perovskite solar cell with a record efficiency of over 18% via hole transport engineering, J. Mater. Sci. Technol. 35 (2019) 987–993, https://doi.org/10.1016/j.jmst.2018.12.025.
[20] S.K.K. Aung, A. Vijayan, T. Seetawan, G. Boschloo, Improved efficiency of perovskite solar cells with low-temperature processed carbon by introduction of a doping-free polymeric hole conductor, Sol. RRL. (2021), 2100773, https://doi.org/10.1002/solr.202100773.
[21] M. Stolterfoht, P. Caprioglio, C.M. Wolff, J.A. Márquez, J. Nordmann, S. Zhang, D. Rothhardt, U. Hörmann, Y. Amir, A. Redinger, L. Kegelmann, F. Zu, S. Albrecht, N. Koch, T. Kirchartz, M. Saliba, T. Unold, D. Neher, The impact of energy alignment and interfacial recombination on the internal and external open-circuit voltage of perovskite solar cells, Energy Environ. Sci. 12 (2019) 2778–2788, https://doi.org/10.1039/c9ee02020a.
[22] E.H. Jung, N.J. Jeon, E.Y. Park, C.S. Moon, T.J. Shin, T.Y. Yang, J.H. Noh, Efficient, stable and scalable perovskite solar cells using poly(3-hexylthiophene), Nature 567 (2019) 511–515, https://doi.org/10.1038/s41586-019-1036-3.
[23] W. Zhang, L. Wan, S. Fu, X. Li, J. Fang, Reducing energy loss and stabilising the perovskite/poly (3-hexylthiophene) interface through a polyelectrolyte interlayer, J. Mater. Chem. A. 8 (2020) 6546–6554, https://doi.org/10.1039/d0ta01860k.
[24] B. Fan, T. You, K. Wang, R. Yin, Y. Gao, L. Huo, P. Yin, Additive-assisted interfacial engineering for efficient carbon-based perovskite solar cell incorporated dopant-free polymeric hole conductor PBDT(S)-T1, ACS Appl. Energy Mater. 4 (2021) 5821–5829, https://doi.org/10.1021/acsaem.1c00631.
[25] Y. Zou, W. Yu, Z. Tang, X. Li, H. Guo, G. Liu, Q. Zhang, Y. Zhang, Z. Zhang, C. Wu, J. Xiao, B. Qu, Z. Chen, L. Xiao, Improving interfacial charge transfer by multi-functional additive for high-performance carbon-based perovskite solar cells, Appl. Phys. Lett. 119 (2021), 151104, https://doi.org/10.1063/5.0061869.
[26] C. Zhi, Z. Li, B. Wei, Recent progress in stabilizing perovskite solar cells through two-dimensional modification, Appl. Phys. Lett. 9 (2021), 070702, https://doi.org/10.1063/5.0056106.
[27] M.A. Mahmud, T. Duong, J. Peng, Y. Wu, H. Shen, D. Walter, H.T. Nguyen, N. Mozaffari, G.D. Tabi, K.R. Catchpole, K.J. Weber, T.P. White, Origin of efficiency and stability enhancement in high-performing mixed dimensional 2D-3D perovskite solar cells: a review, Adv. Funct. Mater. (2021), 2009164, https://doi.org/10.1002/adfm.202009164.
[28] J. Suo, B. Yang, A. Hagfeldt, Passivation strategies through surface reconstruction toward highly efficient and stable perovskite solar cells on n-i-p architecture, Energies 14 (2021) 4836, https://doi.org/10.3390/en14164836.
[29] T. Zhu, D. Zheng, J. Liu, L. Coolen, T. Pauporte, PEAI-based interfacial layer for high-efficiency and stable solar cells based on a macl-mediated grown Fa0.94Ma0.06PbI3 perovskite, ACS Appl. Mater. Interfaces. 12 (2020) 37197–37207, https://doi.org/10.1021/acsami.0c09970.

[30] F. Zheng, C. Zuo, M. Niu, C. Zhou, S.J. Bradley, C.R. Hall, W. Xu, X. Wen, X. Hao, X. Hao, M. Gao, T.A. Smith, K.P. Ghiggino, Revealing the role of methylammonium chloride for improving the performance of 2D perovskite solar cells, ACS Appl. Mater. Interfaces. 12 (2020) 25980–25990, https://doi.org/10.1021/acsami.0c05714.

[31] Q. Jiang, Y. Zhao, X. Zhang, X. Yang, Y. Chen, Z. Chu, Q. Ye, X. Li, Z. Yin, J. You, Surface passivation of perovskite film for efficient solar cells, Nat. Photonics 13 (2019) 460–466, https://doi.org/10.1038/s41566-019-0398-2.

[32] M. Tang, S. Zhang, T.J. Magnanelli, N.V. Nguyen, E.J. Heilweil, T.D. Anthopoulos, C.A. Hacker, Unraveling the compositional heterogeneity and carrier dynamics of alkali cation doped 3D/2D perovskites with improved stability, Mater. Adv. 2 (2021) 1253–1262, https://doi.org/10.1039/d0ma00967a.

[33] M.M. Tavakoli, W. Tress, J.V. Milić, D. Kubicki, L. Emsley, M. Grätzel, Addition of adamantylammonium iodide to hole transport layers enables highly efficient and electroluminescent perovskite solar cells, Energy Environ. Sci. 11 (2018) 3310–3320, https://doi.org/10.1039/c8ee02404a.

[34] S. Wang, Y. Zhu, C. Wang, R. Ma, Interface modification by a multifunctional ammonium salt for high performance and stable planar perovskite solar cells, J. Mater. Chem. A. 7 (2019) 11867–11876, https://doi.org/10.1039/c9ta02631b.

[35] M.J. Jeong, K.M. Yeom, S.J. Kim, E.H. Jung, J.H. Noh, Spontaneous interface engineering for dopant-free poly(3-hexylthiophene) perovskite solar cells with efficiency over 24%, Energy Environ. Sci. 14 (2021) 2419–2428, https://doi.org/10.1039/d0ee03312j.

[36] H. Zhang, Y. Wu, C. Shen, E. Li, C. Yan, W. Zhang, H. Tian, L. Han, W.H. Zhu, Efficient and stable chemical passivation on perovskite surface via bidentate anchoring, Adv. Energy Mater. 9 (2019), 1803573, https://doi.org/10.1002/aenm.201803573.

[37] Z. Wu, M. Jiang, Z. Liu, A. Jamshaid, L.K. Ono, Y. Qi, Highly efficient perovskite solar cells enabled by multiple ligand passivation, Adv. Energy Mater. 10 (2020), 1903696, https://doi.org/10.1002/aenm.201903696.

[38] T. Xu, K. Zou, S. Lv, H. Tang, Y. Zhang, Y. Chen, L. Chen, Z. Li, W. Huang, Efficient and stable carbon-based perovskite solar cells via passivation by a multifunctional hydrophobic molecule with bidentate anchors, ACS Appl. Mater. Interfaces. 13 (2021) 16485–16497, https://doi.org/10.1021/acsami.1c02218.

[39] Y. Liu, Z. Wu, Y. Dou, J. Zhang, T. Bu, K. Zhang, D. Fang, Z. Ku, F. Huang, Y. B. Cheng, J. Zhong, Formamidinium-based perovskite solar cells with enhanced moisture stability and performance via confined pressure annealing, J. Phys. Chem. C 124 (2020) 12249–12258, https://doi.org/10.1021/acs.jpcc.0c02289.

[40] T.J. Jacobsson, J.P. Correa-Baena, E. Halvani Anaraki, B. Philippe, S.D. Stranks, M. E.F. Bouduban, W. Tress, K. Schenk, J. Teuscher, J.E. Moser, H. Rensmo, A. Hagfeldt, Unreacted PbI2 as a double-edged sword for enhancing the performance of perovskite solar cells, J. Am. Chem. Soc. 138 (2016) 10331–10343, https://doi.org/10.1021/jacs.6b06320.

[41] N. Yi, S. Wang, Z. Duan, K. Wang, Q. Song, S. Xiao, Tailoring the performances of lead halide perovskite devices with electron-beam irradiation, Adv. Mater. 29 (2017), 1701636, https://doi.org/10.1002/adma.201701636.

[42] P. Wang, J. Wang, X. Zhang, H. Wang, X. Cui, S. Yuan, H. Lu, L. Tu, Y. Zhan, L. Zheng, Boosting the performance of perovskite solar cells through a novel active passivation method, J. Mater. Chem. A. 6 (2018) 15853–15858, https://doi.org/10.1039/c8ta05593a.

[43] Q. Hu, E. Rezaee, M. Li, Q. Chen, C. Li, S. Cai, H. Shan, Z.X. Xu, P3HT with Zn (C6F5)2 as p-type dopant for the enhanced performance of planar perovskite solar cells, Sol. RRL. 4 (2020), 1900340, https://doi.org/10.1002/solr.201900340.

[44] K. Lee, J. Kim, H. Yu, J.W. Lee, C.M. Yoon, S.K. Kim, J. Jang, A highly stable and efficient carbon electrode-based perovskite solar cell achieved: via interfacial growth of 2D PEA2PbI4 perovskite, J. Mater. Chem. A. 6 (2018) 24560–24568, https://doi.org/10.1039/c8ta09433k.

[45] S.A.A. Shah, M.H. Sayyad, J. Sun, Z. Guo, Hysteresis analysis of hole-transport-material-free monolithic perovskite solar cells with carbon counter electrode by current density–voltage and impedance spectra measurements, Nanomaterials 11 (2021) 48, https://doi.org/10.3390/nano11010048.